

# Space-Time Optimisations for Early Fault-Tolerant Quantum Computation

Sanaa Sharma  
University of Cambridge  
Cambridge, United Kingdom  
ss3241@cam.ac.uk

Prakash Murali  
University of Cambridge  
Cambridge, United Kingdom  
pm830@cam.ac.uk

**Abstract**—Fault-tolerance is the future of quantum computing, ensuring error-corrected quantum computation that can be used for practical applications. Resource requirements for fault-tolerant quantum computing (FTQC) are daunting, and hence, compilation techniques must be designed to ensure resource efficiency. There is a growing need for compilation strategies tailored to the early FTQC regime, which refers to the first generation of fault-tolerant machines operating under stringent resource constraints of fewer physical qubits and limited distillation capacity. Present-day compilation techniques are largely focused on overprovisioning of routing paths and make liberal assumptions regarding the availability of distillation factories. Our work develops compilation techniques that are tailored to the needs of early FTQC systems, including distillation-adaptive qubit layouts and routing techniques. In particular, we show that simple greedy heuristics are extremely effective for this problem, offering up to 60 % reduction in the number of qubits compared to prior works. Our techniques offer results with an average overhead of  $1.2\times$  in execution time for a 53 % reduction in qubits against the theoretical lower bounds. As the industry develops early FTQC systems with tens to hundreds of logical qubits over the coming years, our work has the potential to be widely useful for optimising program executions.

## I. INTRODUCTION

Quantum computers are poised to have practical applications in chemistry, material science, cryptography and other domains [36, 38]. There has been tremendous hardware progress, resulting in noisy quantum computers with hundreds of physical qubits [2, 32]. These systems typically have gate (quantum instruction) error rates greater than  $10^{-3}$ . However, practically useful applications demand qubits with error rates below  $10^{-10}$ . To bridge this gap, quantum error correction (QEC) is required. QEC protects quantum information by encoding the state of a *logical qubit* into several physical qubits and continuously detecting and correcting errors [35]. By combining QEC with *fault-tolerant* operations, we can enable reliable execution of practical quantum applications.

Early fault-tolerant quantum computers (FTQC) are being developed by physically implementing QEC on real hardware [3, 23, 40]. These systems currently have only a handful of logical qubits, with very limited support for running logical operations [34]. In the next five years, we expect systems to have tens to hundreds of logical qubits, with the ability to run several hundred logical gates on them [17, 21, 33]. These systems have unique resource constraints such as limited logical qubit counts, restricted logical qubit connectivity and local instruction sets. To support application executions well,

we require compilation strategies that are tailored to the capabilities of early FTQC systems.

To build early and eventually scalable FTQC systems, one of the most important strategies is based on the *surface code* as the underlying choice of QEC. This code represents logical qubits using a square patch or surface of qubits [11, 13]. It includes a set of physical qubits for storing data and syndrome qubits for determining errors in the logical qubit by repetitive parity check measurements. Google recently demonstrated surface code-based QEC with one logical qubit and academic groups have demonstrated primitive logical operations [3, 4]. However, to realise early scientific applications of quantum computing that are beyond classical computing, we require systems with a few hundred logical qubits [6]. Our work explores how compilation techniques can assist in reducing qubit requirements at this scale.

To reduce qubit requirements, our work focuses on two opportunities. First, logical operations on the surface code are typically local and require very few ancilla qubits [19, 37]. That is, two-qubit operations can be performed between neighbouring (or diagonal) logical qubit with the help of zero, one or two ancillas depending on the operation type. Existing compilation techniques assume that all logical qubits require these ancillas in every timestep, resulting in overprovisioning of ancillas [5, 28]. Second, FTQC requires resource-intensive *magic state distillation* factories and associated routing qubits. Distillation factories are required to implement T gates (a type of non-Clifford gate) that cannot be executed directly on the surface code. Magic state qubits produced using distillation must be routed to the logical qubits when required. Existing compilers either ignore distillation and its routing requirements or assume a large number of distillation factories and overprovision routing paths for them [31].

We develop a compiler for early FTQC systems based on greedy heuristics that reduce qubit requirements through two techniques. First, to reduce qubit requirements during logical operations, we provision a limited number of ancilla qubits. Since quantum operation types are known at compile time, we rearrange data qubits and route ancilla qubits to the desired locations. By scheduling these movement operations in advance, we avoid increasing execution time significantly. Second, we insert a limited number of routing paths and use greedy heuristics to route magic states from the distillation factories to the logical qubits where they are used. Since each

magic state requires several logical cycles to produce, we use this window to pack as many qubit movement operations as possible to hide movement latency. Both techniques rely on determining a minimum set of logical qubit movements either to rearrange ancillas or move magic states. We show that a simple set of greedy heuristics based on a weighted version of Dijkstra’s algorithm [14] is effective for this problem.

We develop our compiler with the IBM Qiskit framework and perform evaluations on a set of early FTQC benchmarks including models for condensed matter simulation and arithmetic circuits. Overall, our contributions are as follows:

- Across benchmarks, our compiler offers an average 53% reduction in logical qubit count, with an average execution time increase of  $1.2\times$ , compared to layouts given in [28]. In comparison with [31], our approach achieves, on average, a  $2\times$  reduction in the spacetime volume with a single distillation factory. Relative to [22], it achieves a 30% reduction in spacetime volume for selected circuits, with more pronounced improvements at higher factory counts.
- We show that it is important to jointly optimise the allocation of routing paths in the compiler and the allocation of magic state factories in the architecture. Compared to Littinski’s fast block layout [28], which assumes a large number of distillation factories, our compiler is *distillation-adaptive*. It reduces spacetime volume by allocating just enough routing paths to prevent bottlenecks from magic state routing.
- Our work enables a richer set of space vs. time tradeoffs compared to prior work which handpicks certain space-time configurations [5, 25, 28, 31]. This is an important capability as we build early FTQC systems, allowing hardware designers to choose configurations that can run on a small number of qubits.

## II. BACKGROUND

### A. Quantum Error Correction and Surface Codes

Quantum error correction is a technique to suppress error in quantum computation by encoding a logical qubit with several physical qubits. When QEC is used, program qubits are mapped to logical qubits in the architecture. Each logical qubit is composed of a number of noisy physical qubits. Works such as [3, 8] describe the successful implementations of QEC and small circuit demonstrations on logical qubits.

One approach to building such quantum computers is based on surface codes. These codes only use nearest-neighbour (NN) interactions in physical qubits for error correction and hence can be implemented on a 2D grid of physical qubits. In a logical qubit encoded with surface codes (Figure 1(b)), there are two types of qubits, data and syndrome, which differ in their function within the code. The data qubits are used for computation, whereas the syndrome qubits are frequently interacted with to conduct parity measurements. Figure 1(a) gives the circuit representation of X and Z syndrome measurements, which ensures that the data qubits are in a simultaneous eigenstate of the operators. The errors in the data qubits are

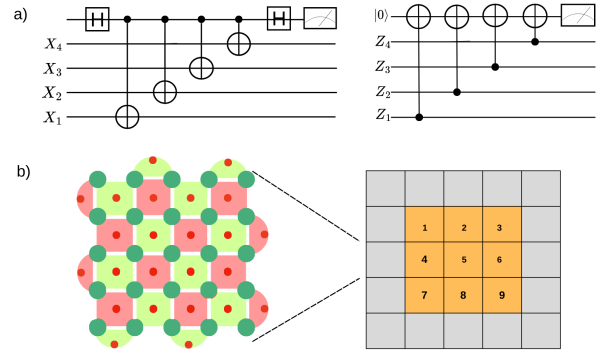


Fig. 1. (a) Circuit representation of X and Z syndrome measurements. (b) (Left) The logical qubit has  $2d^2 - 1$  physical qubits where  $d$  is the code distance (here  $d=5$ ). The big green circles are the data qubits while the small red circles are the syndrome qubits (red and green faces correspond to the Z and X syndromes, respectively). (Right) Layout of logical qubits in the FTQC system. Orange qubits are the logical data qubits, while the grey region consists of logical ancillas, which are used both for instruction implementation and routing magic states.

detected by the syndrome qubits during computation. A single syndrome measurement constitutes one code cycle.

Code distance, in error-correcting codes, is the minimum number of physical qubit errors that can cause a logical error. It is also the number of qubits on one side of the logical qubit. In Figure 1(a), the code distance  $d$  is 5. The larger the code distance, the more errors can be tolerated on the logical level. Code distance affects the execution time of a logical quantum instruction. Each instruction typically requires either  $d$  timesteps or some multiple of  $d$  to ensure fault-tolerance.

### B. Lattice Surgery

Lattice surgery is the standard approach for implementing operations on the surface code [19]. Lattice surgery implements operations non-transversally using the “merge” and “split” techniques while maintaining fault-tolerance across the 2D grid. Figure 2(a) represents a logical qubit as a single qubit cell, with Z and X edges. These edges represent the syndromes on the qubit’s boundaries. The merge and split operations, as shown in Figure 2(b), are the primitive operations that make up the lattice-surgery fault-tolerant operations. Merging is done by measuring joint syndromes across the boundaries of the two qubits during error correction to make a single qubit. Splitting, on the other hand, breaks down a large surface into smaller ones by introducing boundaries.

Figure 2(c) is a circuit decomposition of the lattice surgery-based Controlled NOT (CNOT) operation. CNOT is a common operation in quantum algorithms. The circuit consists of two merge and split operations using measurement operations ( $M_{zz}$  and  $M_{xx}$ ), the outcomes of which are used to apply conditional X and Z operations on the control and target qubits. In Figure 2(d), the lattice surgery operations along with the placement of control, ancilla and target qubits are described. The execution time in lattice surgery operations refers to the number of timesteps required to execute an operation and

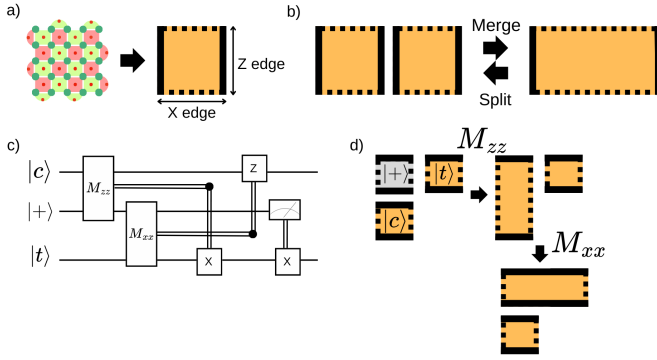


Fig. 2. (a) Logical qubit with X and Z edges. (b) Lattice surgery merge and split operations on two logical qubits. (c) CNOT gate decomposed into lattice surgery primitives. It has a control and a target qubit, given by  $|c\rangle$  and  $|t\rangle$  qubits. The ancilla qubit is  $|+\rangle$ . (d) CNOT operation implementation on two logical qubits and an ancilla.

is proportional to the code distance of the surface codes employed. Our instruction set is described in Section VI.

### C. Magic State Distillation

The surface code natively supports Clifford gates. Non-Clifford gates ( $T$  gates) are implemented through magic state distillation, making them resource-intensive. To implement a  $T$  gate, a magic state of the form  $|0\rangle + e^{i\pi/4}|1\rangle$  is consumed. The natural generation of such states is error-prone, and therefore, a method called *distillation* is used [10, 29]. This method is used to generate higher-fidelity magic states from low-fidelity states via a lengthy protocol. The protocol provides  $T$  states for universal computation and is vital in a fault-tolerant setting. Distillation is conducted separately, and the qubits used in the process are not used for any other type of computation. For many circuits that require  $T$  gates, distillation becomes a major bottleneck that decides the overall time of the computation. Once a magic state is prepared outside the computation block, it is routed close to the data qubits, on which the  $T$  gate needs to be performed. A standard scheme for distillation is called 15-to-1 distillation [10]. It uses 15 input  $T$  states to generate one high-fidelity  $T$  state qubit. This is done in 11 code cycles (11d time steps) of the underlying surface code [28].

### III. RELATED WORK

Given that optimising surface code circuits is known to be NP-hard [18], a variety of optimisation techniques at different levels of abstraction have emerged in recent years [15, 20, 20, 28, 31, 39]. For example, in [28], the entire quantum circuit is decomposed into a set of Pauli-product rotations and measurements. The method uses commutation rules between any two Pauli gates to reduce a quantum program down to a set of multi-qubit non-Clifford operations and multi-qubit measurements. This method offers a promising solution for circuits with a large set of operations, as it manages to ultimately decompose them into a single set of Pauli-product operations. However, the latency (and increased qubit cost) of

implementing multi-qubit Pauli product operations in different block layouts is not evaluated [30]. Hence, it does not provide a complete picture of the compilation procedure that takes into account the physical constraints of performing large multi-qubit Pauli product operations. In other works such as [5, 31], methods are described to optimise paths implementing two-qubit operations and for routing magic states. These methods help define the depth of a particular circuit for certain layouts, which is crucial for performing 2-qubit gates. However, certain bottlenecks, such as distillation processing time, are not accounted for. Other NISQ compilers, such as [24, 27], describe techniques for reducing computational overhead but do not address challenges related to distillation routing.

### IV. PROBLEM STATEMENT

As mentioned in section I, surface code compilation faces two major sources of overhead. First, although logical operations on the surface code are inherently local and often require few ancilla qubits, existing compilers liberally assume that ancillas are needed for every logical qubit in every timestep, leading to systematic overprovisioning. For example, in the compact block of [31], the ratio of data to ancilla qubits is 1:3, thereby imposing significant demands on qubit resources. Second, magic state distillation and routing constitute a major bottleneck: distillation factories are highly resource-intensive but essential for implementing non-Clifford gates such as the  $T$  gate, and the distilled states must be routed efficiently to their target logical qubits. Existing compilers often either neglect these requirements entirely or operate under the assumption of abundant distillation capacity and routing paths, an assumption that is unrealistic in early fault-tolerant settings. In [6, 20, 28, 31], distillation bottlenecks are not considered, and the proposed compilation schemes are developed without explicit optimisation for resource-constrained architectures.

This motivates the following questions:

- Given the critical bottlenecks in surface code compilation, what represents the most resource-efficient balance, and how can optimisation techniques be structured to manage the trade-off between qubit overhead and execution time?
- At the architectural level, how can we incorporate properties of early fault-tolerant systems such as limited distillation capabilities and routing paths during compilation?

These questions motivate the development of a compiler capable of optimising trade-offs between qubits and execution time while incorporating architectural constraints that reflect the resource limitations.

### V. METHODS

Our compilation scheme takes as input a quantum program expressed in the Clifford+ $T$  gate set. The pipeline comprises three stages: mapping, routing, and scheduling. At the end of this process, the compiler produces a circuit that is compatible with implementation on the surface code. In the mapping stage, the circuit qubits are assigned to a 2D grid of logical qubits. This grid accommodates both the qubits required for the circuit itself and the additional ancilla qubits necessary

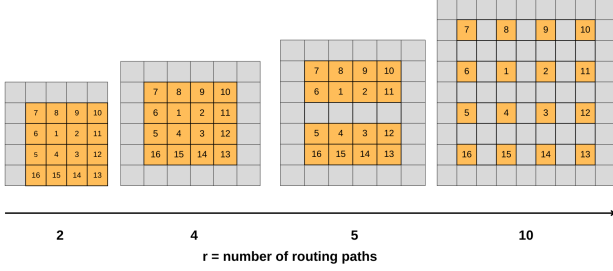


Fig. 3. Qubit layouts generated as a function of routing paths. The data qubits are in orange, while the bus qubits are in grey.

to support logical operations and routing. Within the mapping stage, the grid is parameterised by the number of routing paths. These routing paths are created by assigning rows/columns of bus qubits, which can also be used as operational ancilla. In Figure 3, a circuit with 16 data qubits (in orange) is shown. The routing paths, depicted in grey, represent the bus qubits placed around the data qubits, going from 2 to 10. For instance, the first subfigure in Figure 3 includes two edges of bus qubits (top and left), corresponding to two routing paths. The subsequent layout extends this to four routing paths, formed by the four edges surrounding the data qubits. In comparison to prior works discussed in Section IV, where the ratio of data to ancilla qubits is typically 1:2 or 1:3, our layouts (with  $r = 3, 4$ ) achieve a more resource-efficient ratio of approximately 2:1. We increase routing paths by inserting columns or rows of bus qubits between the data qubits. These paths are required to perform lattice surgery operations, which need special configurations to execute. More routing paths increase the total number of qubits used in compilation but make it easier for operations to run in parallel, consequently reducing the overall time.

We assign an initial static mapping to our grid depending on the 1D/2D programs. Although limited optimisation is performed at this stage, the total execution time benefits from adopting a layout that is aligned with the gate dependencies in the application. We consider a range of 2D circuits derived from condensed matter models such as the Ising, Heisenberg, and Fermi–Hubbard Hamiltonians. These circuits are important for early FTQC since they represent applications which are scientifically interesting and beyond classical computing. Additionally, their Hamiltonians are defined by NN interactions between spins, which map naturally onto logical qubits arranged on a 2D grid in fault-tolerant architectures. When translated into quantum circuits, these NN interactions are represented by CNOT gates between pairs of qubits, accompanied by additional single-qubit operations. Similarly, a 1D Ising model benefits from a snake-like mapping that preserves NN interactions, consistent with those specified in the input circuit.

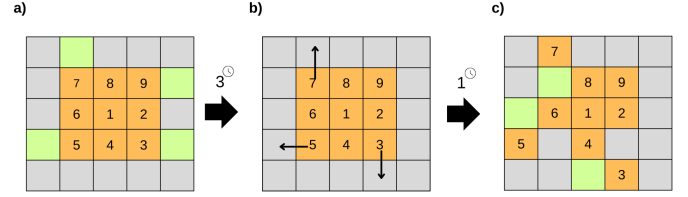


Fig. 4. Neighbour-dependent moves inspect neighbouring qubits to determine the appropriate move operation. Before the CNOT operations, qubits labelled 3, 5, 7, and 9 undergo a Hadamard operation simultaneously (a). Following this, the data qubits consult the circuit’s directed acyclic graph (DAG) to determine the subsequent move operations. In this instance, the upcoming gates are three CNOTs applied to qubit pairs (3, 4), (5, 6), and (7, 8). To prepare for these interactions, the data qubits move to adjacent positions, enabling diagonal placement (b). The ancilla qubits positioned between each control–target pair are highlighted in neon. The Hadamard operation requires three timesteps, whereas each move operation requires one timestep.

The primary optimisation is performed during the routing phase, where we employ an adapted version of Dijkstra’s algorithm for efficient path-finding [14], combined with gate-dependent moves for neighbouring qubits. For our ancilla-optimised layouts (with  $r = 3, 4$ ), it is crucial to minimise the number of move operations across the 2D grid during circuit implementation. Our approach ensures minimal disturbance to the 2D layout while maintaining operational efficiency.

#### A. Gate-dependent moves in the neighborhood

Building up on the ideas discussed in the previous section, we now look at the compilation techniques used in this work. Gate-dependent moves constitute a form of look-ahead compilation, wherein, after applying an operation to a given data qubit, the compiler examines subsequent operations in the circuit before deciding the qubit’s movement. The heuristic takes the *directed acyclic graph* (DAG) of the quantum circuit as input, applies gates to qubits that satisfy the placement constraints (for example, CNOT needs a control and target qubit in a diagonal position with ancilla in between, as shown in Figure 7). It then determines the next set of move operations for these qubits. An illustrative example is provided in Fig. 4, where the first panel applies an H operation to four data qubits simultaneously (ancilla qubits highlighted in neon). Subsequent move decisions are then made to ensure that the following layer of operations, which involves a CNOT gate, respects the placement constraints. In the example shown, qubit labels 3, 5, and 7 move to positions diagonal to 4, 6, and 8, respectively, to enable a CNOT between them.

#### B. Find a path using Dijkstra’s algorithm

In our construction, the move operations are essential to the compilation scheme, as data qubits need to be configured correctly. Pathfinding is, therefore, the most important heuristic

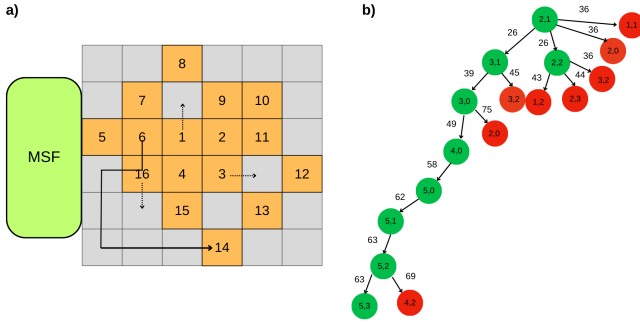


Fig. 5. The starting position is qubit 6 at coordinates (2,1), and the target position is qubit 14 at (5,3). As illustrated in (a), the path looks for minimum disturbance on the grid. Figure (b) shows the corresponding decision tree, where the green cells indicate the optimal movement path. The red cells indicate the rejected cells. The cost of each movement is given on the edge and cells with the minimum cost are chosen.

because of the large number of move operations that need to be made. We use Dijkstra’s algorithm implemented with binary heap priority queue data structures to efficiently select the next qubit to process. The algorithm minimises a cost function to determine a near-optimal path. Our pathfinding algorithm is used to route magic states, move data qubits for CNOTs, and find unoccupied cells for lattice surgery operations. The cost function in the algorithm is given by:

$$C(a, b) = d(a, b) * p \quad (1)$$

where  $d(a,b)$  is the distance between  $a$  and  $b$ , and  $p$  is the penalty factor. The penalty factor is defined as the number of cells that are occupied by data qubits along a given path. It plays a crucial role because, in a dense 2D grid, the goal is to identify paths that minimise disturbance to other data qubits. The algorithm explores neighbouring cells and assigns a specific penalty cost to each potential move. Movement to an unoccupied cell incurs zero cost, whereas moves over occupied cells accrue a penalty. This procedure effectively creates a decision tree that is dynamically updated each time a cell is moved. A simple example illustrating this process is provided in Fig. 5.

### C. Space Search

Space search is employed to determine an appropriate placement of ancilla for a specific gate operation. The algorithm takes as input the location of the target qubit and the operation to be applied. It then searches the 2D grid for the nearest unoccupied cell that can be used as a degree of freedom in the congested grid, moving the occupied cells one step at a time. This creates the necessary space for the operation, and the appropriate path is found using Dijkstra’s algorithm with the preset cost function. Fig. 6 illustrates an example of a space search in a densely packed grid. The ancilla position that requires the fewest moves to clear is selected to minimise overall time overhead.

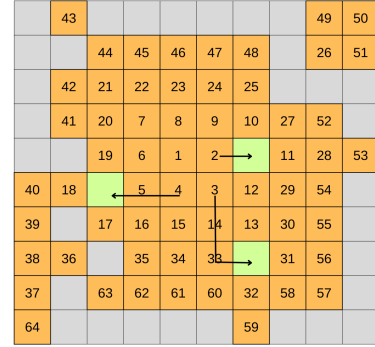


Fig. 6. Space search identifies unoccupied cells around data qubits in order to create space within an ancilla-optimised layout while minimising the number of move operations. In the example shown, the data qubit labelled ‘1’ undergoes a Hadamard operation, and three neighbouring data cells are available for movement. Since the Hadamard gate requires only a single ancilla, relocating the qubit labelled ‘2’ is the most efficient option.

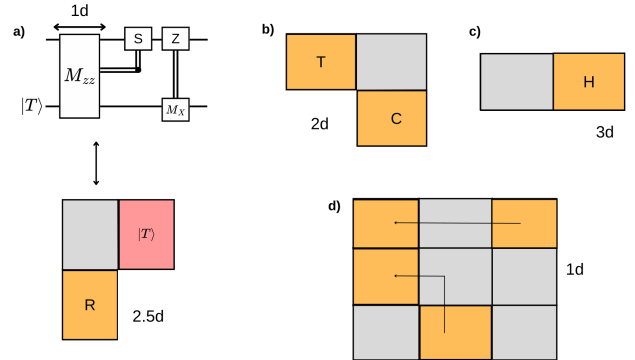


Fig. 7. Latticery surgery operations with their configurations and timesteps. Data qubits are given in orange, ancilla in grey and the magic state in pink. (a) T gate is applied in 2.5d timesteps, where a single  $M_{zz}$  operation takes 1d timestep, followed by an S gate. (b) CNOT gate is applied using a control (C) and a target (T) qubit. (c) Hadamard assumes one ancilla and is performed in 3d timesteps. (d) Move operation takes 1d timestep.

### D. Remove Redundant Moves

This layer of optimisation is carried out in the scheduling stage. The DAG, which is generated finally from the methods above, is used to find commuting move operations such that  $U_{r_i \rightarrow r_j}^\dagger U_{r_j \rightarrow r_i} = I$ , where  $r_i, r_j$  correspond to the initial and final positions of the move operation. Since greedy heuristics make decisions based on the immediate achievable placement of data qubits, many redundant move operations can be identified and eliminated, thereby further reducing the overall execution time.

## VI. EVALUATION

### A. Experimental Setup

**Instruction set:** In Figure 7, we describe the operations used by our compilation method and the time cost associated with them. We assume an instruction set where operations are allowed only between sets of logical qubits which are adjacent [16, 22]. This instruction set choice eases implementation

Model	Gate Count	Qubits
Ising 2D	CNOT : 360, $R_Z$ : 280, H : 300	100
Heisenberg 2D	H : 1440, CNOT : 1080, $R_Z$ : 540, S : 360, $S^\dagger$ : 360	100
Fermi Hubbard 2D	H : 400, CNOT : 300, S : 100, $S^\dagger$ : 100; $R_Z$ : 150	100
GHZ	CNOT : 254, $R_Z$ : 2, SX : 34, X : 1	255
Adder	$R_Z$ : 240, CNOT : 195, SX : 48, X : 13	28
Multiplier	$R_Z$ : 300, CNOT : 222, SX : 34, X : 4	15

TABLE I  
GATE COUNTS FOR DIFFERENT BENCHMARK CIRCUITS.

requirements for early FTQC systems. Following prior works, we mention the time cost per operation to be a multiple of the code distance ( $d$ ) [6, 28]. For example, a) T state consumption circuit shows an  $M_{zz}$  operation along with S gate [28]. The  $M_{zz}$  operation in lattice surgery takes  $1d$  code cycle, and the S gate takes another  $1.5d$  code cycles [7]. (b) CNOT takes  $2d$  timesteps because of  $M_{zz}$  and  $M_{xx}$  operations [12] and (c) Hadamard takes  $3d$  timesteps [7, 9]. Finally, (d) Move operation takes  $1d$  timesteps [5].

**Placement constraints:** The placement of the data and ancilla qubits during an operation is crucial for the implementation. A logical qubit has both X and Z edges, and only relevant sides can participate in  $M_{xx}$  and  $M_{zz}$  operations. For example, the control and target qubits (as given in Figures 2 and 7) should be diagonal with a neighbouring ancilla to perform both  $M_{zz}$  and  $M_{xx}$  operations, respectively. In our scheme, we do not account for rotations, as we assume additional edge constraints, allowing merge operations to take place only at relevant positions such that the top and bottom edges correspond to Z syndromes, while the left and right edges are the X syndromes. Therefore,  $M_{ZZ}$  operations only occur vertically, whereas  $M_{XX}$  operations occur horizontally.

**Benchmarks:** We use a set of 18 quantum programs and compare our work with three state of the art FTQC compilation techniques. Our benchmarks are given in Table I. They include condensed matter Hamiltonians across system sizes ranging from 4 to 100 qubits (specifically 4, 16, 36, 64, and 100), though in the table we report only the maximum dimension. The circuits used for these condensed matter Hamiltonians are all single Trotter step implementations.

**Lower bound calculation:** We consider a set of qubit layouts by varying the number of routing paths (as shown in Fig. 3) and assess our results relative to a theoretical lower bound in execution time. Our lower bound ( $l$ ) is calculated by the formula:

$$l = \frac{n_T * t_{MSF}}{n_{MSF}} \quad (2)$$

where  $n_T$  is the number of T states required in a quantum circuit,  $t_{MSF}$  is the processing time to produce a single magic state and  $n_{MSF}$  is the number of factories assumed in the

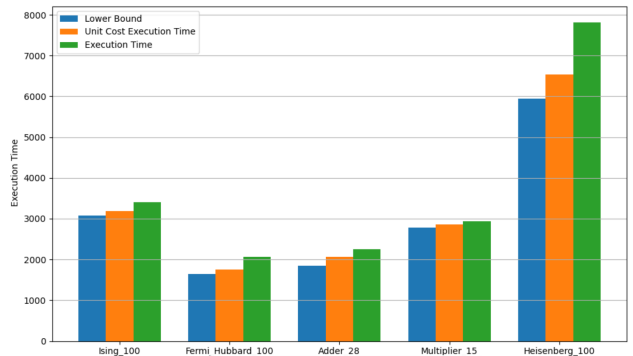


Fig. 8. Unit cost execution time is the total time calculated while assigning a unit cost to all the operations in the compiler scheme. Execution time refers to the actual time considering realistic operation latencies. On average, we record an increase of roughly  $1.2\times$  in the execution time compared to the lower bound.

compilation process. Since our focus is on early fault-tolerant systems, we do not assume an abundance of magic states. Instead, we explicitly account for delays arising from their processing time. The magic state processing time is taken to be  $11d$  timesteps [28]. The lower bound describes an ideal scenario where the only bottleneck determining the execution time is the preset distillation processing time, ensuring no further room for optimisation in the compilation.

## VII. RESULTS

### A. Execution time analysis with respect to lower bounds

In Figure 8, the bar chart shows results of five benchmarks. The condensed matter circuits are all single Trotter step quantum implementations with 100 qubits. The results are presented for a specific qubit layout with  $r = 4$  (Figure 3). This layout was selected as it yields promising results by incurring only minimal overhead in execution time. We compare our lower bound with both the execution time and the unit cost execution time. The execution time is the overall time taken to run the computation, while the unit cost execution time refers to the total time calculated by assigning a unit cost ( $1d$  timestep) to all operations in lattice surgery. This allows us to evaluate the proximity of our method to the ideal scenario where the only bottleneck in the circuit is the magic state processing time. In the case of condensed matter circuits, the unit cost execution time for Ising and Fermi Hubbard circuits is only  $1.1\times$ - $1.2\times$  of the lower bound, while it is slightly higher ( $1.3\times$ ) for the Heisenberg circuit. The total execution time (i.e., the time calculated by assuming realistic operation latency) is increased by a factor of  $1.2$  to  $1.4$  for the three circuits. In the multiplier circuit, the execution time is only  $1.06\times$  the lower bound. Overall, our compiler offers execution times that are very close to the lower bound.

### B. Distillation-adaptive routing path allocation

Figure 9 has three plots depicting the spacetime product v/s the number of distillation factories while varying the

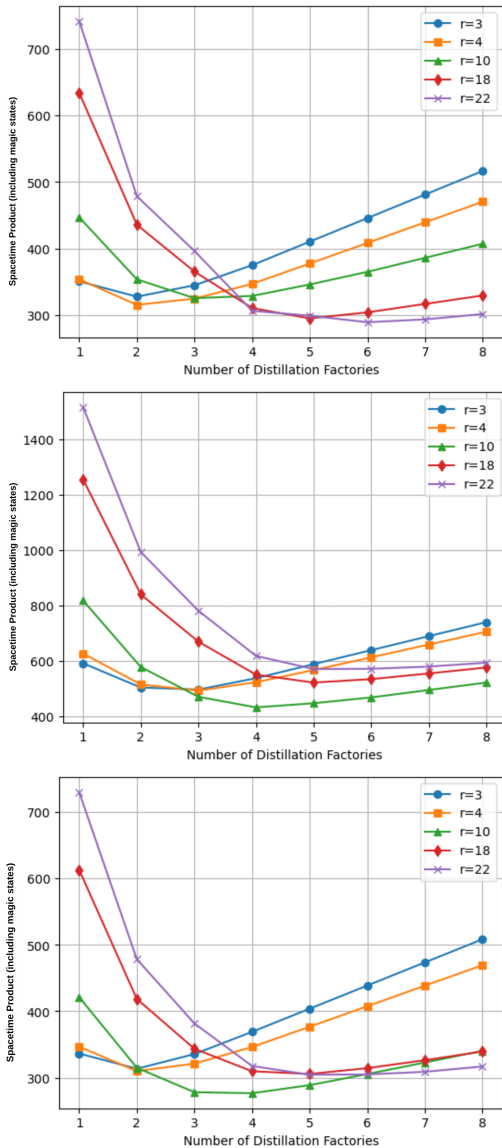


Fig. 9. Spacetime volume (including magic states) per operation versus the number of distillation factories, with routing paths varied as specified in Figure 3. Top: 10x10 Fermi-Hubbard model. Middle: 10x10 Ising model. Bottom: 10x10 Heisenberg Model. The parameter ‘r’ denotes the number of routing paths. The trend shows that more routing paths are needed to see the effects of a greater factory count. For  $r = 3$ , two factories are optimal, but for  $r = 22$ , five factories give the lowest spacetime volume.

routing paths. In these plots, the spacetime product includes distillation qubits and accounts for the total spacetime volume of computation. Each curve in the plot provides us with an optimal number of distillation factories for a layout with a given number of routing paths. We observe that the curves are U-shaped, owing to the trade-off between the number of qubits and execution time. The number of distillation factories is directly proportional to the number of qubits, and we observe that with too few qubits (fewer factories), runtime dominates. As we increase the factory count, time decreases, but qubit overhead dominates. The optimum lies in between, where

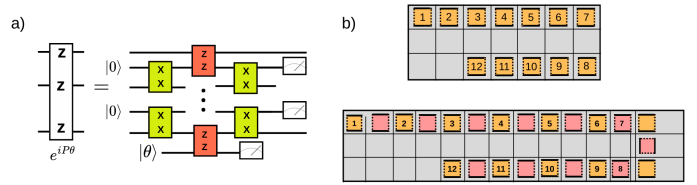


Fig. 10. (a) Constant depth decomposition of Pauli-Product Rotations ( $e^{iP\theta}$ ) using  $n$  ancillary qubits. (b) To run the same operations in a compact layout, new ancillary spaces are added (in pink). The bus qubits (grey) are then used as routing paths. The total number of qubits increases to  $3n+3$ .

execution time and qubit count balance out. For example, in the Fermi-Hubbard 2D case (top), provisioning two distillation factories for layouts with 3-4 routing paths gives the optimal spacetime volume. When the routing paths (and qubits) are increased, 5-6 distillation factories are optimum ( $r = 18, 22$ ). As the number of routing paths in the grid increases, greater flexibility is available for routing magic states, thereby making the impact of multiple distillation factories more pronounced. We also observe a marked shift in the spacetime volume when increasing the number of factories from one to eight. For the Heisenberg circuit (bottom), when operating with a single magic state factory, the spacetime volume at code distance  $r = 22$  is approximately  $2.16\times$  that at  $r = 3$ . In contrast, with eight factories, this relationship is inverted: the spacetime volume at  $r = 22$  is reduced to about  $0.62\times$  the corresponding value at  $r = 3$ .

Moreover, our compiler offers the ability to determine the optimal combination of factory count and routing paths for each application. For the Ising and Heisenberg circuits, a routing path length  $r = 10$  yields the lowest spacetime volume, whereas for the Fermi-Hubbard circuit the minimum occurs only when the number of routing paths exceeds 18. This variation occurs due to the differences in the instruction mix across applications. More magic states require more routing paths to relieve routing congestion and achieve low space-time volume. By optimising these choices and reducing resource requirements, our work has the potential to enable early FTQC applications sooner.

### C. Comparison with Game of Surface Codes

We evaluate our scheme against selected existing methods in the literature, comparing both qubit count and execution time. We draw comparisons with techniques from [22, 28, 31]. In Figure 11, we compare the results from [28], using its compact and fast block layouts. The execution time of Pauli Product Rotations (PPRs) is determined by first decomposing the PPRs into two-body XX and ZZ interactions, as given in [30]. PPRs are large logical operations that comprise hundreds of qubits in a layout. Such operations are difficult to implement and are decomposed into nearest-neighbour operations assuming hardware connectivities. The decomposition described in [30] incurs an additional constant depth latency and requires twice the number of ancillary qubits for implementation (shown in Figure 10(a)). To understand the realistic implementation of

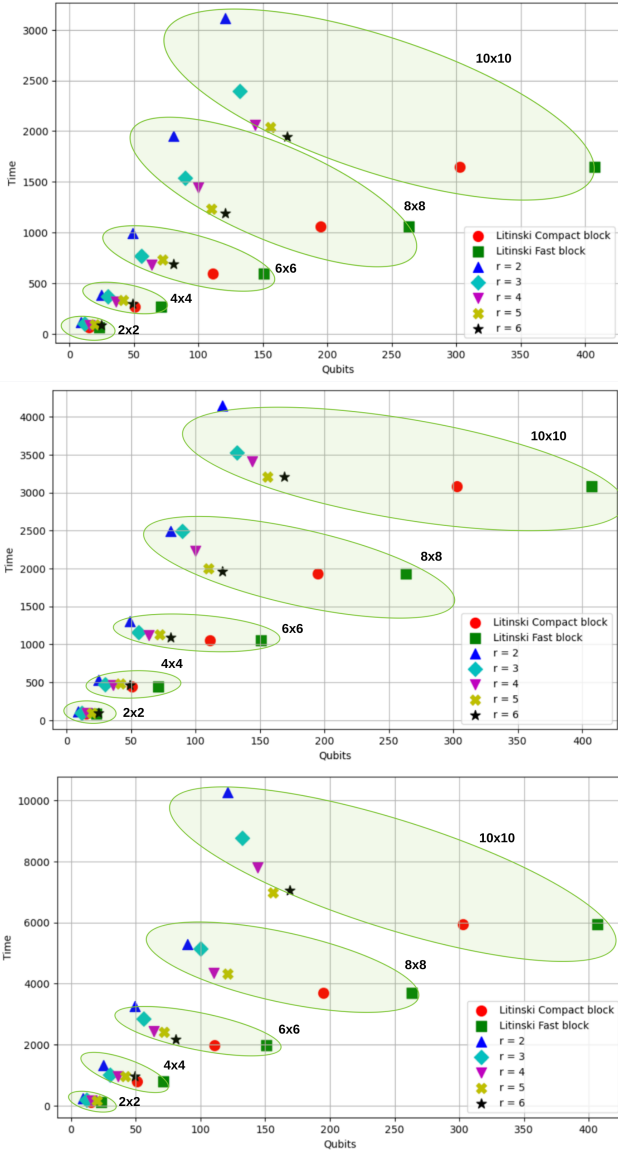


Fig. 11. Execution time v/s qubit plots with one distillation factory and single Trotter step: (Top) Fermi-Hubbard, (Middle) Ising, and (Bottom) Heisenberg model circuits, evaluated across problem sizes with routing paths as specified in Figure 3. The green circles indicate the problem sizes. Our results are compared with the compact and fast block layouts of [28], under the assumption of constant-depth decomposition for large Pauli product rotations.

these PPRs, we introduce ancillary qubits in the layout design and calculate the spacetime cost accordingly. In the case of the compact block layout (Figure 10(b)), this decomposition increases the number of qubits from  $1.5n+3$  to  $3n+3$ , where  $n$  is the number of data qubits. Similarly, for intermediate and fast blocks, the total qubits in these layouts increase to  $4n$  and  $4n+6$  when used for realistic implementations. The new layouts and implementations of  $e^{i\theta Z^{\otimes n}}$  are given in Appendix A.

We note that the PPRs generated by moving the Cliffords using [1] are not all  $P = Z^{\otimes n}$  for unitary gates of the form  $e^{iP\theta}$ . Condensed matter Hamiltonians generate PPRs where

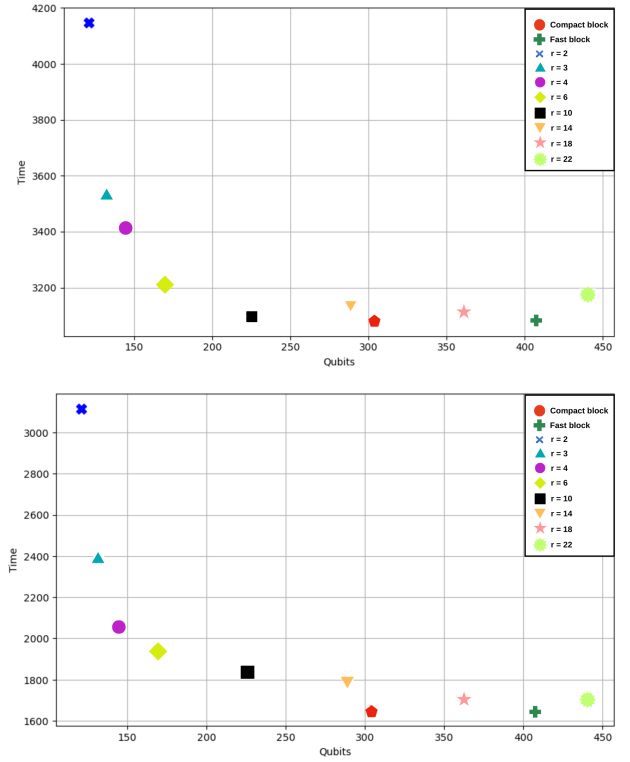


Fig. 12. Execution time v/s qubit plots with one distillation factory and single Trotter step: (Top) Ising, (Bottom) Fermi-Hubbard model circuits, evaluated for  $10 \times 10$  Hamiltonians with routing paths as specified in Figure 3. The results are compared against the fast and compact blocks. We obtain optimal results at  $r=10$  with an execution time overhead of  $1.04 \times$  for the Ising circuit and at  $r=6$  with an overhead of  $1.1 \times$  for the Fermi-Hubbard circuit.

$P = X^{\otimes n}, Y^{\otimes n}$  and  $P = Z \otimes I \dots \otimes Z$  among others. In particular, for rotations of the form  $e^{i\theta Z \otimes I \dots \otimes Z}$ , the presence of identity operators between the non-trivial terms would, in practice, require additional SWAP operations (and qubits), effectively mapping the gate onto a next-nearest-neighbour architecture. For the sake of generality, however, we do not account for this overhead and instead assume an equal number of timesteps for all multi-qubit Pauli-product rotations of the form  $e^{iP\theta}$ .

While the decomposition significantly increases the number of total qubits for the compact, intermediate and fast blocks, it doesn't affect the total time. This is because the magic state processing time is greater than the operation execution time. Nevertheless, the latency of such operations could become significant in cases where the magic state processing time is improved, more than one distillation factory is used or when SWAP gates are included to implement  $P = e^{iZ \otimes I \dots \otimes Z}$  operations. However, in this case, the execution time of the PPR approach in all three layouts coincides with the lower bound presented in Equation 2.

As shown in Figure 11, we run our compilation technique on single Trotter step circuits of Fermi-Hubbard 2D, Ising 2D and Heisenberg 2D circuits. The circuit size is increased from 4 to 100 qubits, and the number of distillation factories is set

to 1 (at 11d timesteps). We compare the resulting execution time (y-axis) from our techniques as a function of the qubit count (x-axis) with both compact and fast block layouts. The legends represent the number of routing paths in the layout. We observe that layouts with  $r = 5$  and 6 are the most optimal, achieving minimal execution time increase as compared to compact and fast blocks, while offering a large reduction in qubit count. For 2D Ising programs, we see that the modified intermediate and fast blocks from [28]’s scheme have more than twice the number of qubits used in our approaches, with an average reduction of only about 20% in overall time. For the 100-qubit Fermi–Hubbard, Ising, and Heisenberg circuits, our best-case results achieve execution time overheads of roughly  $1.22\times$ ,  $1.04\times$ , and  $1.17\times$ , respectively, while reducing qubit requirements by 53%. This reduces the qubit count close to the optimal level, yielding a substantial reduction that brings the data-to-ancilla qubit ratio to approximately 3:1.

In Figure 12, we generate the execution time v/s qubit plots for 10x10 qubit Ising (top) and Fermi-Hubbard (bottom) circuits by varying the routing paths. We begin with 2 routing paths that have bus qubits aligned across 2 edges of the grid. The maximum number of routing paths in our layouts is  $2n+2$ , where  $n$  is the number of data qubits. In this case, the maximum number of routing paths is 22, which is  $3\times$  the number of ancillary qubits per data qubit. Results show that the optimal range to implement these circuits is between 4 and 6 routing paths, which corresponds to 144-169 qubits. The overall time in compact and fast blocks is the same as the lower bound and is the lowest in the curve. Our method, with the same number of qubits as the compact and fast block ( $\sim 400$ ), has an overall time  $1.03\times$  more than the lower bound. We note that our technique is able to generate better, near-optimal results in conditions with a constrained set of resources, i.e., less provisioning of qubits.

#### D. Comparison with LSQCA

In Figure 13, we compare qubit cost, execution time, and the spacetime volume against the LSQCA approach presented in [22]. The referenced work proposes a load/store quantum computer architecture and evaluates two designs, namely the Point SAM (Scan-Access Memory) and the Line SAM. As reported in the paper, the Line SAM architecture reduces latency significantly by increasing the number of scan cells; therefore, we compare our results against this more optimal design. We evaluate the condensed matter quantum circuits and include additional benchmarks from [26] given in Table I. Except for the GHZ circuit, all other circuits contain T gates and require magic state routing. The execution time is compared using *CPI* (cycles per instruction), defined as the total execution time divided by the number of operations in the input circuit. *CPI* helps us assess how efficiently the techniques execute instructions independent of the program size. In Figure 13, we compare the most optimal layouts for each benchmark for comparisons. The magic state factory is fixed at one, with processing time taking 11d timesteps.

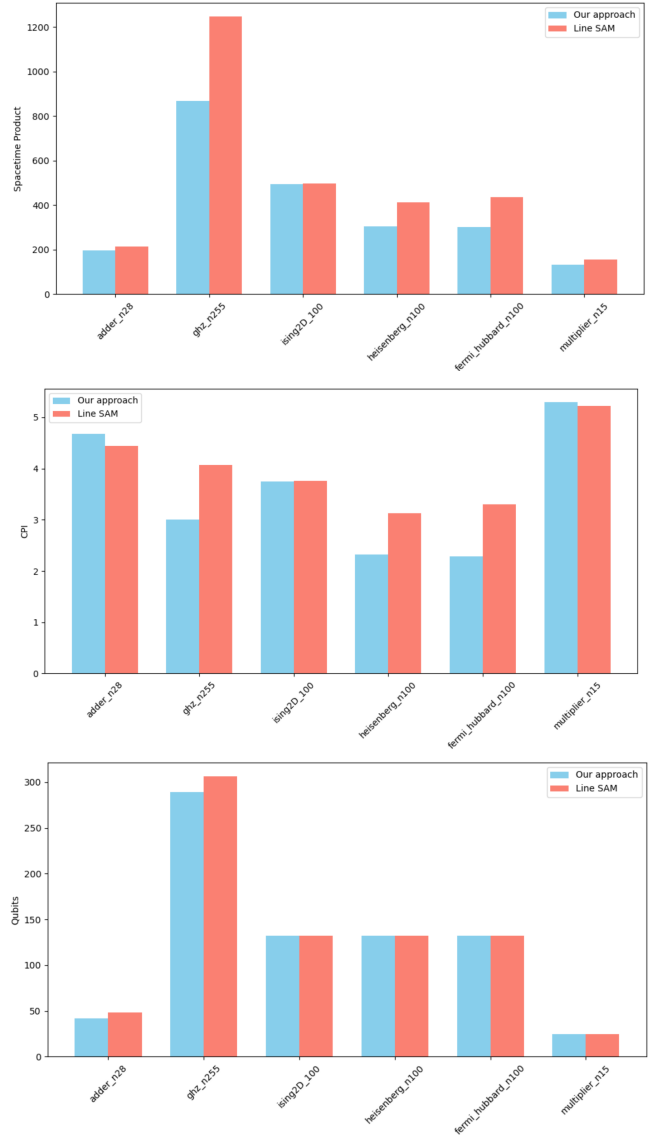


Fig. 13. Comparison with the Line-SAM method of [22] with a single distillation factory. The top plot compares the spacetime volume of both approaches across the benchmarks listed in Table I. The middle and bottom plots present the corresponding qubit counts and execution times, respectively. We get, on an average, a 20% decrease in spacetime volume across all benchmarks.

We further examine the impact of varying the number of factories and the processing time of magic states on the execution time in both approaches. In Figure 14(a, b, c), we compare the cost per instruction to execute 100 qubit Fermi-Hubbard, Ising and Heisenberg 2D circuits, respectively, with an increase in the number of factories from 1 to 4. The sequential nature of Line SAM prevents a reduction in execution time as the number of factories increases. This is because, while the T state availability is improved with the number of factories, the movement of data qubits between regions takes up a significant amount of time. For the Ising 2D circuit with one factory, the execution time of Line SAM is  $1.0029\times$  that of

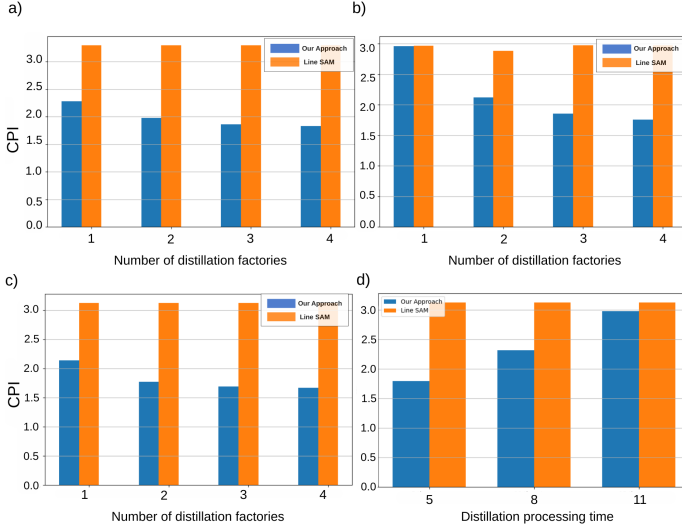


Fig. 14. Comparison with the Line-SAM method of [22]. (a–c) present CPI results for  $10 \times 10$  circuits of the Fermi–Hubbard, Ising, and Heisenberg models, as the number of magic state distillation factories is increased from 1 to 4. (d) For the  $10 \times 10$  Ising circuit, the bar graph shows the effect of varying the magic state processing time.

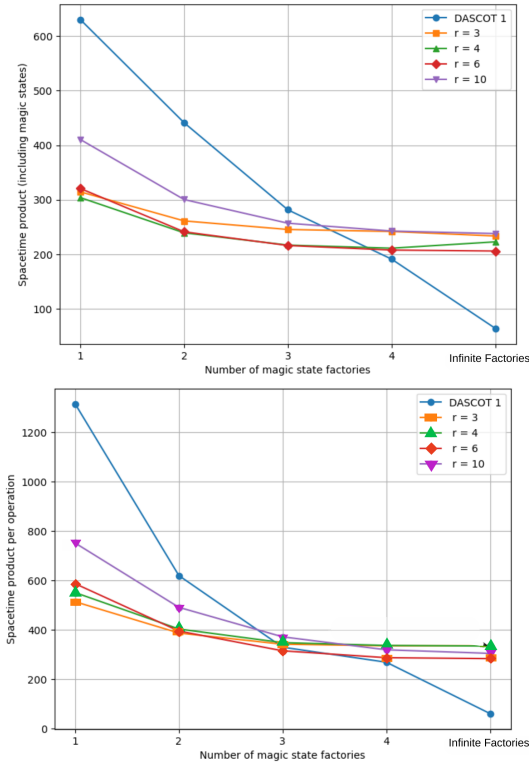


Fig. 15. Comparison with DASCOT method of [31]. Spacetime volume versus the number of distillation factories, with routing paths varied as specified in Figure 3. Top:  $10 \times 10$  Fermi–Hubbard model. Bottom:  $10 \times 10$  Ising model. The parameter ‘ $r$ ’ denotes the number of routing paths. In this plot, spacetime volume excludes magic state factories because of DASCOT’s assumption of unlimited factories.

our approach, which increases to  $1.6898 \times$  when four factories are used. In 14(d), we study the change in the CPI as we vary the distillation processing times for the Ising circuit. We observe that reducing the processing time leads to a substantial decrease in time overheads for our approach relative to Line SAM. This improvement arises because Line SAM permits considerably less parallelism within the circuit. Consequently, it achieves near-optimal performance only when the magic state processing bottleneck is sufficiently large to dominate all other sequential operations in the architecture.

### E. Comparison with DASCOT

We compare our results with DASCOT [31]’s results. DASCOT exploits dependency structures between circuit operations to optimise for mapping and routing problems. This method only deals with routing for two-qubit operations and magic states and generates steps for implementing these operations from a circuit in parallel. While the approach generates near-optimal results for routing, the layout described in the paper uses  $3 \times$  more qubits than our layouts. Figure 15 is a plot of the spacetime volume per operation as a function of the number of factories. The two figures correspond to the single Trotter step  $10 \times 10$  Fermi–Hubbard 2D (top) and Ising 2D (bottom) models while changing the available routing paths. The first entry (blue) is the DASCOT result for the compact layout. DASCOT assumes an unlimited supply of magic states and does not incorporate the bottlenecks associated with state distillation when generating the execution steps. Moreover, it does not use “move” operations because it is a compilation technique used to route CNOTs and T states. However, for our comparison, we introduce the compilation bottleneck as an added constraint in the result and compare for different numbers of factories. We consider factory counts ranging from 1 to 4; in addition, a fifth data point represents the scenario with infinite factories. Results show that when there is an abundance of T states, the spacetime product of the DASCOT approach is the lowest. At this point, the spacetime product of our approach is, on average,  $4.7 \times$  more than that of DASCOT. However, as we introduce the distillation constraints, DASCOT’s spacetime volume increases relative to our results. This is because while DASCOT’s routing method is able to parallelise operations through routing, it is unable to perform T gates with a reduced availability of T states due to the architecture constraints. At one factory in the 2D Fermi–Hubbard circuit (top), the DASCOT spacetime product averages at  $1.96 \times$  the spacetime product from our approach (averaged over the routing paths).

## VIII. CONCLUSION

Early FTQC systems are expected to be developed in the next five years. Yet, compilation techniques for fault-tolerant quantum are focused on the long term with minimum resource constraints. Our work considers the compilation challenge for early FTQC systems and contributes heuristics that offer large improvements in qubit counts and spacetime volumes for important quantum applications compared to prior works. Surprisingly, we show that very simple greedy heuristics come

close to optimal performance in these metrics. As systems scale up, our work has the potential to be an important part of the compilation toolchain and inform software design.

#### REFERENCES

- [1] (2025). Pauli product measurement. <https://pennylane.ai/compilation/pauli-product-measurement>.
- [2] AbuGhanem, M. (2025). Ibm quantum computers: evolution, performance, and future directions. *The Journal of Supercomputing*, 81(5):687.
- [3] Acharya, R., Abanin, D. A., Aghababaie-Beni, L., Aleiner, I., Andersen, T. I., Ansmann, M., Arute, F., Arya, K., Asfaw, A., Astrakhantsev, N., Atalaya, J., Babbush, R., Bacon, D., Ballard, B., Bardin, J. C., Bausch, J., Bengtsson, A., Bilmes, A., Blackwell, S., Boixo, S., Bortoli, G., Bourassa, A., Bovaird, J., Brill, L., Broughton, M., Browne, D. A., Buchea, B., Buckley, B. B., Buell, D. A., Burger, T., Burkett, B., Bushnell, N., Cabrera, A., Campero, J., Chang, H.-S., Chen, Y., Chen, Z., Chiaro, B., Chik, D., Chou, C., Claes, J., Cleland, A. Y., Cogan, J., Collins, R., Conner, P., Courtney, W., Crook, A. L., Curtin, B., Das, S., Davies, A., De Lorenzo, L., Debroy, D. M., Demura, S., Devoret, M., Di Paolo, A., Donohoe, P., Drozdov, I., Dunsworth, A., Earle, C., Edlich, T., Eickbusch, A., Elbag, A. M., Elzouka, M., Erickson, C., Faoro, L., Farhi, E., Ferreira, V. S., Burgos, L. F., Forati, E., Fowler, A. G., Foxen, B., Ganjam, S., Garcia, G., Gasca, R., Genois, É., Giang, W., Gidney, C., Gilboa, D., Gosula, R., Dau, A. G., Graumann, D., Greene, A., Gross, J. A., Habegger, S., Hall, J., Hamilton, M. C., Hansen, M., Harrigan, M. P., Harrington, S. D., Heras, F. J. H., Heslin, S., Heu, P., Higgott, O., Hill, G., Hilton, J., Holland, G., Hong, S., Huang, H.-Y., Huff, A., Huggins, W. J., Ioffe, L. B., Isakov, S. V., Iveland, J., Jeffrey, E., Jiang, Z., Jones, C., Jordan, S., Joshi, C., Juhas, P., Kafri, D., Kang, H., Karamlou, A. H., Kechedzhi, K., Kelly, J., Khaira, T., Khatyar, T., Khezri, M., Kim, S., Klimov, P. V., Klots, A. R., Kobrin, B., Kohli, P., Korotkov, A. N., Kostritsa, F., Kothari, R., Kozlovskii, B., Kreikebaum, J. M., Kurilovich, V. D., Lacroix, N., Landhuis, D., Lange-Dei, T., Langley, B. W., Laptev, P., Lau, K.-M., Le Guevel, L., Ledford, J., Lee, J., Lee, K., Lensky, Y. D., Leon, S., Lester, B. J., Li, W. Y., Li, Y., Lill, A. T., Liu, W., Livingston, W. P., Locharla, A., Lucero, E., Lundahl, D., Lunt, A., Madhuk, S., Malone, F. D., Maloney, A., Mandrà, S., Manyika, J., Martin, L. S., Martin, O., Martin, S., Maxfield, C., McClean, J. R., McEwen, M., Meeks, S., Megrant, A., Mi, X., Miao, K. C., Mieszala, A., Molavi, R., Molina, S., Montazeri, S., Morvan, A., Movassagh, R., Mruzckiewicz, W., Naaman, O., Neeley, M., Neill, C., Nersisyan, A., Neven, H., Newman, M., Ng, J. H., Nguyen, A., Nguyen, M., Ni, C.-H., Niu, M. Y., O’Brien, T. E., Oliver, W. D., Opremcak, A., Ottosson, K., Petukhov, A., Pizzuto, A., Platt, J., Potter, R., Pritchard, O., Pryadko, L. P., Quintana, C., Ramachandran, G., Reagor, M. J., Redding, J., Rhodes, D. M., Roberts, G., Rosenberg, E., Rosenfeld, E., Roushan, P., Rubin, N. C., Saei, N., Sank, D., Sankaragomathi, K., Satzinger, K. J., Schurkus, H. F., Schuster, C., Senior, A. W., Shearn, M. J., Shorter, A., Shu, N., Shvarts, V., Singh, S., Sivak, V., Skrzynny, J., Small, S., Smelyanskiy, V., Smith, W. C., Somma, R. D., Springer, S., Sterling, G., Strain, D., Suchard, J., Szasz, A., Szein, A., Thor, D., Torres, A., Torunbalci, M. M., Vaishnav, A., Vargas, J., Vdovichev, S., Vidal, G., Villalonga, B., Heidweiller, C. V., Waltman, S., Wang, S. X., Ware, B., Weber, K., Weidel, T., White, T., Wong, K., Woo, B. W. K., Xing, C., Yao, Z. J., Yeh, P., Ying, B., Yoo, J., Yosri, N., Young, G., Zalcman, A., Zhang, Y., Zhu, N., Zobrist, N., AI, G. Q., and Collaborators (2025). Quantum error correction below the surface code threshold. *Nature*, 638(8052):920–926.
- [4] Andersen, C. K., Remm, A., Lazar, S., Krinner, S., Lacroix, N., Norris, G. J., Gabureac, M., Eichler, C., and Wallraff, A. (2020). Repeated quantum error detection in a surface code. *Nature Physics*, 16(8):875–880.
- [5] Beverland, M., Kliuchnikov, V., and Schoute, E. (2022a). Surface code compilation via edge-disjoint paths. *PRX Quantum*, 3:020342.
- [6] Beverland, M. E., Murali, P., Troyer, M., Svore, K. M., Hoefler, T., Kliuchnikov, V., Low, G. H., Soeken, M., Sundaram, A., and Vaschillo, A. (2022b). Assessing requirements to scale to practical quantum advantage.
- [7] Blunt, N. S., Gehér, G. P., and Moylett, A. E. (2024). Compilation of a simple chemistry application to quantum error correction primitives. *Phys. Rev. Res.*, 6:013325.
- [8] Bluvstein, D., Evered, S. J., Geim, A. A., Li, S. H., Zhou, H., Manovitz, T., Ebadi, S., Cain, M., Kalinowski, M., Hangleiter, D., Bonilla Ataides, J. P., Maskara, N., Cong, I., Gao, X., Sales Rodriguez, P., Karolyshyn, T., Semeghini, G., Gullans, M. J., Greiner, M., Vuletić, V., and Lukin, M. D. (2024). Logical quantum processor based on reconfigurable atom arrays. *Nature*, 626(7997):58–65.
- [9] Bombín, H., Dawson, C., Mishmash, R. V., Nickerson, N., Pastawski, F., and Roberts, S. (2023). Logical blocks for fault-tolerant topological quantum computation. *PRX Quantum*, 4:020303.
- [10] Bravyi, S. and Kitaev, A. (2005). Universal quantum computation with ideal clifford gates and noisy ancillas. *Phys. Rev. A*, 71:022316.
- [11] Bravyi, S. B. and Kitaev, A. Y. (1998). Quantum codes on a lattice with boundary.
- [12] Decker, E., Goetz, L., McKinney, E., Gustafson, E., Zhou, J., Liu, Y., Jones, A., Li, A., Schuckert, A., Stein, S., Crane, E., and Li, G. (2025). Kernpiler: Compiler optimization for quantum hamiltonian simulation with partial trotterization.
- [13] Dennis, E., Kitaev, A., Landahl, A., and Preskill, J. (2002). Topological quantum memory. *Journal of Mathematical Physics*, 43(9):4452–4505.
- [14] Dijkstra, E. W. (1959). A note on two problems in connexion with graphs. *Numerische Mathematik*, 1(1):269–271.
- [15] Ding, Y., Holmes, A., Javadi-Abhari, A., Franklin, D.,

- Martonosi, M., and Chong, F. T. (2018). Magic-state functional units: mapping and scheduling multi-level distillation circuits for fault-tolerant quantum architectures. In *Proceedings of the 51st Annual IEEE/ACM International Symposium on Microarchitecture*, MICRO-51, page 828–840. IEEE Press.
- [16] Fowler, A. G., Mariantoni, M., Martinis, J. M., and Cleland, A. N. (2012). Surface codes: Towards practical large-scale quantum computation. *Phys. Rev. A*, 86:032324.
- [17] Google (2024). Google roadmap. <https://quantumai.google/roadmap>.
- [18] Herr, D., Nori, F., and Devitt, S. J. (2017). Optimization of lattice surgery is np-hard. *npj Quantum Information*, 3(1):35.
- [19] Horsman, D., Fowler, A. G., Devitt, S., and Meter, R. V. (2012). Surface code quantum computing by lattice surgery. *New Journal of Physics*, 14(12):123011.
- [20] Hua, F., Chen, Y., Jin, Y., Zhang, C., Hayes, A., Zhang, Y., and Zhang, E. Z. (2021). Autobraid: A framework for enabling efficient surface code communication in quantum computing. In *MICRO-54: 54th Annual IEEE/ACM International Symposium on Microarchitecture*, MICRO '21, page 925–936, New York, NY, USA. Association for Computing Machinery.
- [21] IBM (2024). Ibm quantum roadmap. <https://www.ibm.com/quantum/technology>.
- [22] Kobori, T., Suzuki, Y., Ueno, Y., Tanimoto, T., Todo, S., and Tokunaga, Y. (2025). Lsqca: Resource-efficient load/store architecture for limited-scale fault-tolerant quantum computing. In *2025 IEEE International Symposium on High Performance Computer Architecture (HPCA)*, pages 304–320.
- [23] Krinner, S., Lacroix, N., Remm, A., Di Paolo, A., Genois, E., Leroux, C., Hellings, C., Lazar, S., Swiadek, F., Herrmann, J., Norris, G. J., Andersen, C. K., Müller, M., Blais, A., Eichler, C., and Wallraff, A. (2022). Realizing repeated quantum error correction in a distance-three surface code. *Nature*, 605(7911):669–674.
- [24] Lao, L. and Browne, D. E. (2022). 2qan: a quantum compiler for 2-local qubit hamiltonian simulation algorithms. In *Proceedings of the 49th Annual International Symposium on Computer Architecture*, ISCA '22, page 351–365, New York, NY, USA. Association for Computing Machinery.
- [25] Lao, L., Wee, B. v., Ashraf, I., Someren, J. v., Khammassi, N., Bertels, K., and Almudever, C. G. (2018). Mapping of lattice surgery-based quantum circuits on surface code architectures. *Quantum Science and Technology*, 4(1):015005.
- [26] Li, A., Stein, S., Krishnamoorthy, S., and Ang, J. (2022). Qasmbench: A low-level quantum benchmark suite for nisq evaluation and simulation. *ACM Transactions on Quantum Computing*.
- [27] Li, G., Ding, Y., and Xie, Y. (2019). Tackling the qubit mapping problem for nisq-era quantum devices. In *Proceedings of the Twenty-Fourth International Conference on Architectural Support for Programming Languages and Operating Systems*, ASPLOS '19, page 1001–1014, New York, NY, USA. Association for Computing Machinery.
- [28] Litinski, D. (2019a). A Game of Surface Codes: Large-Scale Quantum Computing with Lattice Surgery. *Quantum*, 3:128.
- [29] Litinski, D. (2019b). Magic State Distillation: Not as Costly as You Think. *Quantum*, 3:205.
- [30] Moffic, I. and Paler, A. (2024). On the Constant Depth Implementation of Pauli Exponentials.
- [31] Molavi, A., Xu, A., Tannu, S., and Albarghouthi, A. (2025). Dependency-aware compilation for surface code quantum architectures. *Proc. ACM Program. Lang.*, 9(OOP-SLA1).
- [32] Patra, S., Jahromi, S. S., Singh, S., and Orús, R. (2024). Efficient tensor network simulation of ibm’s largest quantum processors. *Phys. Rev. Res.*, 6:013326.
- [33] Quantinuum (2024). Quantinuum quantum computing roadmap. <https://www.quantinuum.com/press-releases/quantinuum-unveils-accelerated-roadmap-to-achieve-universal-fault-tolerant-quantum-computing-by-2030>.
- [34] Reichardt, B. W., Paetznick, A., Aasen, D., Basov, I., Bello-Rivas, J. M., Bonderson, P., Chao, R., van Dam, W., Hastings, M. B., Mishmash, R. V., Paz, A., da Silva, M. P., Sundaram, A., Svore, K. M., Vaschillo, A., Wang, Z., Zanner, M., Cairncross, W. B., Chen, C.-A., Crow, D., Kim, H., Kindem, J. M., King, J., McDonald, M., Norcia, M. A., Ryou, A., Stone, M., Wadleigh, L., Barnes, K., Battaglini, P., Bohdanowicz, T. C., Booth, G., Brown, A., Brown, M. O., Cassella, K., Coxe, R., Epstein, J. M., Feldkamp, M., Griger, C., Halperin, E., Heinz, A., Hummel, F., Jaffe, M., Jones, A. M. W., Kapit, E., Kotru, K., Lauigan, J., Li, M., Marjanovic, J., Megidish, E., Meredith, M., Morshead, R., Muniz, J. A., Narayanaswami, S., Nishiguchi, C., Paule, T., Pawlak, K. A., Pudenz, K. L., Pérez, D. R., Simon, J., Smull, A., Stack, D., Urbanek, M., van de Veerdonk, R. J. M., Vendeiro, Z., Weverka, R. T., Wilkason, T., Wu, T.-Y., Xie, X., Zaly-Geller, E., Zhang, X., and Bloom, B. J. (2025). Fault-tolerant quantum computation with a neutral atom processor.
- [35] Shor, P. W. (1995). Scheme for reducing decoherence in quantum computer memory. *Phys. Rev. A*, 52:R2493–R2496.
- [36] Shor, P. W. (1997). Polynomial-time algorithms for prime factorization and discrete logarithms on a quantum computer. *SIAM Journal on Computing*, 26(5):1484–1509.
- [37] Thomsen, F., Kesselring, M. S., Bartlett, S. D., and Brown, B. J. (2024). Low-overhead quantum computing with the color code. *Phys. Rev. Res.*, 6:043125.
- [38] von Burg, V., Low, G. H., Häner, T., Steiger, D. S., Reiher, M., Roetteler, M., and Troyer, M. (2021). Quantum computing enhanced computational catalysis. *Phys. Rev. Res.*, 3:033055.
- [39] Watkins, G., Nguyen, H. M., Watkins, K., Pearce, S., Lau, H.-K., and Paler, A. (2024). A High Performance Compiler for Very Large Scale Surface Code Computations. *Quantum*, 8:1354.

[40] Zhao, Y., Ye, Y., Huang, H.-L., Zhang, Y., Wu, D., Guan, H., Zhu, Q., Wei, Z., He, T., Cao, S., Chen, F., Chung, T.-H., Deng, H., Fan, D., Gong, M., Guo, C., Guo, S., Han, L., Li, N., Li, S., Li, Y., Liang, F., Lin, J., Qian, H., Rong, H., Su, H., Sun, L., Wang, S., Wu, Y., Xu, Y., Ying, C., Yu, J., Zha, C., Zhang, K., Huo, Y.-H., Lu, C.-Y., Peng, C.-Z., Zhu, X., and Pan, J.-W. (2022). Realization of an error-correcting surface code with superconducting qubits. *Phys. Rev. Lett.*, 129:030501.

## APPENDIX

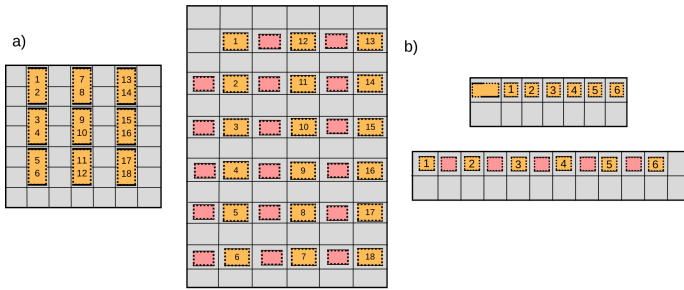


Fig. 16. New intermediate and fast layouts. The total number of qubits in these layouts is  $4n$  and  $4n+6$ , respectively.

Pauli Product rotations of the form  $e^{i\theta Z^{\otimes n}}$  are implemented on compact, intermediate and fast block layouts (from [28]) by adding more ancillary qubits to the layouts. The new layouts for the intermediate and fast blocks are given in Figure 16. The total number of qubits in the new layouts is  $4n$  and  $4n+6$ . These operations are implemented with a constant depth (3d timesteps) as given in Figure 10. Due to layout constraints, this time can be slightly more in some cases. One such example is given in Figure 17. Nearest-neighbour XX and ZZ operations take 1d timestep. However, because of the overlapping of routing paths, the nearest-neighbour ZZ operations take 2d timesteps. Therefore, the total time required to perform a PPR for the compact block is 4d timesteps. For the new intermediate and fast block layouts, there are enough routing paths to allow all XX and ZZ operations to be performed simultaneously. The total timesteps to implement the PPR operations of the form  $e^{i\theta Z^{\otimes n}}$  is 3d timesteps.

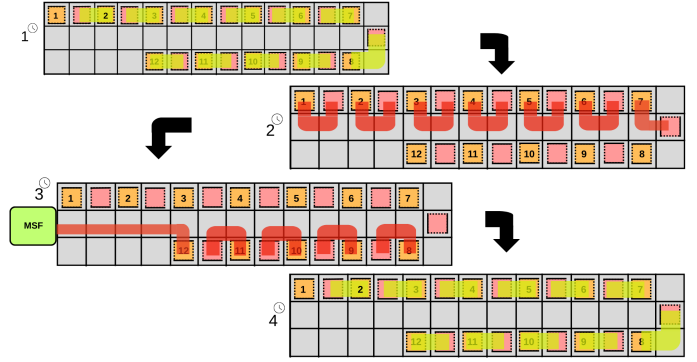


Fig. 17. Routing of XX and ZZ two-qubit measurements in the compact block. The XX operations (along with the routing paths) are shown in green, while the ZZ operations are shown in red. Time taken to implement a  $Z^{\otimes n}$  operation in a compact block is 4d code cycles.